Supporting Online Material

Structural Basis for Activation of Class Ib Ribonucleotide Reductase

Amie K. Boal,[1] Joseph A. Cotruvo, Jr.,[2] JoAnne Stubbe,[2,3,*] and Amy C. Rosenzweig[1,*]

[1]Departments of Biochemistry, Molecular Biology and Cell Biology and of Chemistry, Northwestern University, Evanston, IL 60208

[2]Departments of Chemistry and [3]Biology, Massachusetts Institute of Technology, Cambridge, MA 02139

[*]To whom correspondence should be addressed. E-mail: stubbe@mit.edu, amyr@northwestern.edu

Materials and Methods

General crystallographic methods. All data sets were processed using the HKL2000 package (*S1*) and solved by molecular replacement using the program PHASER (*S2*). Model building and refinement were performed with Coot (*S3*) and Refmac5 (*S4*), respectively. Data collection and refinement statistics are shown in Tables S1 and S2. Ramachandran plots were calculated with PROCHECK (*S5*) and diffraction-component precision index (DPI) errors were calculated with SFCHECK (*S6*). Figures were prepared using PyMOL (*S7*) and channel calculations were performed with HOLLOW (*S8*). All data were collected at the Life Sciences Collaborative Access Team (LS-CAT) beamlines at the Advanced Photon Source (APS).

Mn^{II}_2-NrdF structure. Apo NrdF from *Escherichia coli* was prepared as described previously (*S9, S10*). Mn^{II}_2-NrdF was generated via incubation of apo NrdF (30 mg/mL in 50 mM HEPES pH 7.6, 5% glycerol) with four molar equivalents of $MnCl_2$ on ice for 20 min. Hexagonal prism-shaped crystals were obtained using the sitting drop vapor diffusion method at 20 °C with 30% (w/v) PEG 4000, 0.1 M HEPES pH 7.5 as a precipitant. Crystals were soaked in cryoprotectant solution (30% (w/v) PEG 4000, 0.1 M HEPES pH 7.5) for less than 5 min, mounted on rayon loops, and flash cooled in liquid nitrogen.

The structure was solved using the coordinates of *Salmonella typhimurium* Fe^{II}_2-NrdF (PDB accession code 1R2F) (*S11*) as the initial model. The final model consists of residues 5-288, two Mn^{II} ions, one glycerol molecule, and 400 water molecules. As observed in all other class I β2 structures, the last 32 residues are not observed in the electron density map and were not modeled. Ramachandran plots indicate that 100% of the residues are in the allowed and additionally allowed regions, and the DPI error is 0.067 Å. Anomalous difference Fourier maps

calculated using data collected at the Mn^{II} absorption edge (Mn^{II}_2-NrdF anomalous, Table S1) reveal strong density at both Mn^{II} sites, and both were modeled at full occupancy.

Fe^{II}_2-NrdF structure. Apo NrdF from *E. coli* (20 mg/mL in 50 mM HEPES pH 7.6, 5% glycerol) was crystallized via hanging drop vapor diffusion at room temperature in 25% (w/v) PEG 4000, 0.1 M HEPES pH 7.6, 0.1 M Li_2SO_4. Hexagonal prism-shaped crystals were transferred to a 10 μL cryoprotectant solution (35% (w/v) PEG 4000, 0.1 M HEPES pH 7.6, 0.1 M Li_2SO_4) and mixed with an additional 10 μL cryoprotectant (as above) aliquot containing 8 mM $Fe(NH_4)_2(SO_4)_2$ and 8 mN sulfuric acid. The crystals were soaked for 5 min, during which the pH of the drop remained between 7 and 8. Crystals were then mounted on rayon loops and flash frozen in liquid nitrogen.

The structure was solved using the coordinates of Mn^{II}_2-NrdF as a starting model. The final model consists of residues 6-287, two Fe^{II} ions, and 154 water molecules. Ramachandran plots indicate that 100% of the residues are in the allowed and additionally allowed regions, and the DPI error is 0.107 Å. Anomalous difference Fourier maps calculated using data collected at the Fe^{II} absorption edge (Fe-NrdF anomalous, Table S1) reveal strong peaks at both sites, but both were best modeled at an occupancy of 0.5. The occupancy was adjusted to minimize residual density observed in F_o-F_c maps. A similar soaking procedure using $MnCl_2$ yielded a structure identical to the Mn^{II}_2-NrdF co-crystal structure described above with the Mn^{II} sites modeled at 0.9 occupancy. The average protein B factors for Fe^{II}_2-NrdF are higher than those observed for Mn^{II}_2-NrdF (Table S1). This likely reflects the difference in how the structures were obtained (Fe^{II}_2-NrdF by crystallization of apo-NrdF followed by soaking with Fe^{II} versus Mn^{II}_2-NrdF by cocrystallization). The average protein B factors for a Mn^{II}_2-NrdF structure obtained by soaking with Mn^{II} are similar to those of the Fe^{II}_2-NrdF structure.

$NrdI_{ox}$/NrdF structure. Apo NrdF and N-terminally His_6-tagged NrdI proteins were prepared as described previously (*S9, S10*), and NrdF was loaded with Mn^{II} as described above. NrdI in 20 mM HEPES pH 7.0, 5% glycerol was concentrated to 22 mg/mL in a Microcon (Amicon) centrifugal concentrator at 4 °C in the presence of 5 mM β-mercaptoethanol to reduce an intermolecular disulfide bond (non-physiologically relevant). An equimolar amount of Mn^{II}_2-NrdF was added to NrdI along with additional β-mercaptoethanol to a final concentration of 5 mM. Bright yellow crystals (22 mg/mL total protein) were obtained using the hanging drop vapor diffusion method with 20% (w/v) PEG 3000, 0.1 M HEPES pH 7.6, 0.1 M lithium sulfate as the precipitant. Crystals were soaked in cryoprotectant solution (30% (w/v) PEG 3000, 0.1 M HEPES pH 7.6) for less than 5 min, mounted on rayon loops, and flash cooled in liquid nitrogen.

The structure was solved using the coordinates of Mn^{II}_2-NrdF and *Bacillus subtilis* NrdI (PDB accession code 1RLJ) as the initial model. The final model consists of residues 6-288 for NrdF chain A, 6-287 for NrdF chain B, residues 3-130 for each NrdI chain, four Mn^{II} ions, two flavin mononucleotide (FMN) cofactors, and 20 water molecules. In this structure and in all other complex structures described below, residual electron density extending from the C-terminus of NrdF along the surface of NrdI was observed in the $2F_o$-F_c and F_o-F_c maps but could not be modeled. Ramachandran plots indicate that 100% of the residues are in the allowed and additionally allowed regions, and the DPI error is 0.326 Å. All four Mn^{II} sites in the asymmetric unit were modeled at full occupancy with minimal density around the metal center observed in F_o-F_c maps.

$NrdI_{hq}$/NrdF structure. The $NrdI_{hq}$/NrdF complex was generated as described previously (*S9, S10*). Briefly, NrdI (20 mM HEPES pH 7.0, 5% glycerol) was concentrated to 22 mg/mL and degassed on a Schlenk line with 5 cycles of evacuation and purging with argon

gas. All subsequent manipulations, including crystallization, were carried out in an anaerobic chamber (Coy Laboratory Products). NrdI was reduced with 2 molar equivalents of sodium dithionite and immediately mixed with an equimolar amount of degassed Mn^{II}_2-NrdF. Some precipitation was evident upon addition of dithionite to NrdI and was removed by brief centrifugation after complex formation. Colorless crystals were obtained by hanging drop vapor diffusion at room temperature using 0.1 M HEPES pH 7.0, 20% (w/v) PEG 3000, 0.2 M Li_2SO_4 as the precipitant. Ten molar equivalents of sodium dithionite (3 mM) were added to the wells immediately prior to drop setup. Crystals were soaked briefly in cryoprotectant solution in the anaerobic chamber (35% PEG (w/v) 3000, 0.1 M HEPES pH 7.0, 0.1 M Li_2SO_4) and immediately flash cooled in liquid nitrogen.

The structure was solved using $NrdI_{ox}$/NrdF as a starting model. The final model consists of residues 6-287 for each NrdF chain, residues 3-133 NrdI chain C, residues 3-130 for NrdI chain D, four Mn^{II} ions, two FMN cofactors, and 280 water molecules. Ramachandran plots indicate that 100% of the residues are in the allowed and additionally allowed regions, and the DPI error is 0.147 Å. All Mn^{II} sites were modeled at full occupancy.

$NrdI_{hq}$/$NrdF_{perox}$ structure. $NrdI_{ox}$/NrdF crystals were obtained as described above. These crystals were soaked in cryoprotectant solution (35% PEG (w/v) 4000, 0.1 M HEPES pH 7.6, 0.1 M Li_2SO_4) containing 100 mM sodium dithionite under ambient conditions for ~2 min and immediately flash cooled in liquid nitrogen. The structure was solved using $NrdI_{ox}$/NrdF as the initial model. The final model consists of residues 5-288 for each NrdF chain, residues 3-131 for each NrdI chain, four Mn^{II} ions, two FMN cofactors, two peroxide molecules, and 168 water molecules. Ramachandran plots indicate that 100% of the residues are in the allowed and

additionally allowed regions, and DPI error is 0.280 Å. All four Mn^{II} sites were modeled at full occupancy.

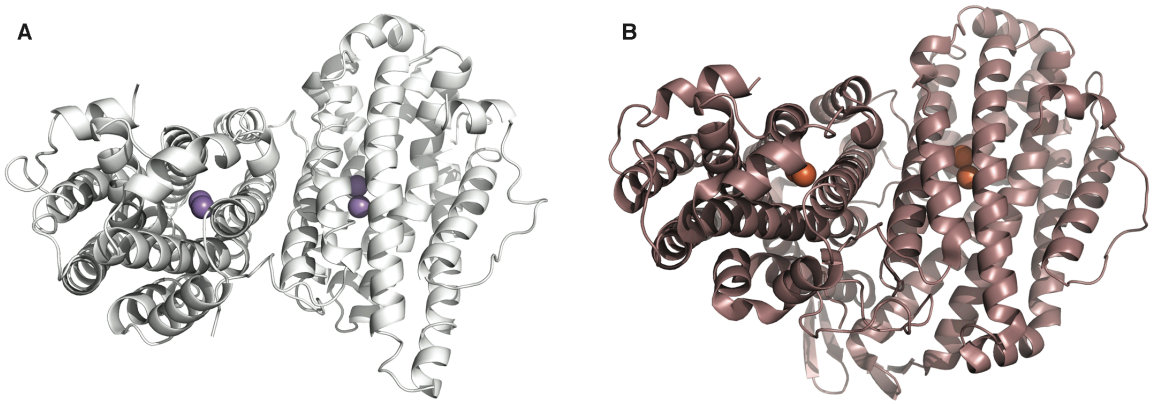

Figure S1. Comparison of the overall structure of *E. coli* Mn^{II}_2-NrdF (class Ib) to that of Fe^{II}_2-NrdB (class Ia) (PDB code 1PIY). (**A**) Mn^{II}_2-NrdF is shown as a white ribbon diagram and the Mn^{II} ions are shown as purple spheres. Mn^{II}_2-NrdF crystallizes with one monomer per asymmetric unit. The biological dimer is generated by crystallographic symmetry. (**B**) Fe^{II}_2-NrdB is shown as a pink ribbon diagram and the Fe^{II} ions are shown as orange spheres.

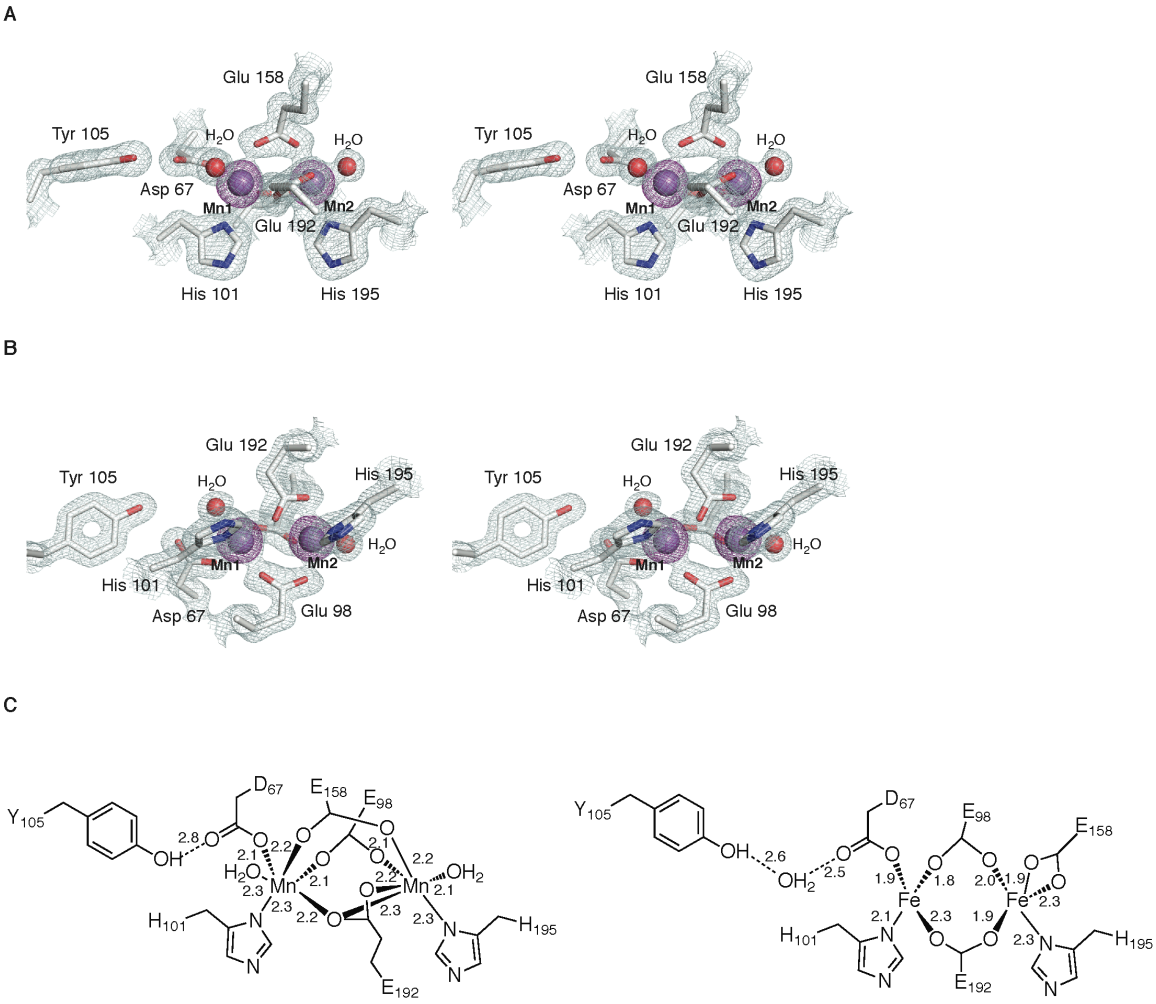

Figure S2. Additional representations of the coordination environments in Mn^{II}_2- and Fe^{II}_2-NrdF. Mn^{II}_2-NrdF displays a completely atypical coordination mode for Glu 158 and one distinct from that of Fe^{II}_2-NrdF for Glu 192. In addition, coordinated solvent is evident in Mn^{II}_2-NrdF at both the Mn1 and Mn2 sites. As stated in the main text, observation of two coordinated solvent molecules in a Mn^{II}_2 or Fe^{II}_2 β2 structure is unusual and such molecules are not evident in Fe^{II}_2-NrdF, though the Fe^{II} atoms are modeled at 50% occupancy in this structure. However, coordinated solvent is also absent in the structures of class Ia *E. coli* Fe^{II}_2 β2 and *C. ammoniagenes* Fe^{II}_2-NrdF which were obtained similarly with Fe^{II} atoms modeled at full occupancy in at least one subunit (*S12, S13*). (**A**) A $2F_o$-F_c electron density map (light blue mesh, contoured at 1.8σ) is shown for residues and solvent molecules in the first coordination sphere along with Tyr 105, the site of the stable tyrosyl radical in NrdF. Mn^{II} ions are shown as purple spheres, water molecules are shown as red spheres, and NrdF side chains are represented in stick format and colored by atom type. An anomalous difference map calculated using data collected at the Mn absorption edge is superimposed (purple mesh, contoured at 18σ). (**B**) An alternate view of (**A**) highlighting the μ-(η^1,η^2) bridging interaction between Glu 192 and the Mn^{II}_2 site. (**C**) Diagram of metal-ligand and hydrogen bonding interactions in Mn^{II}_2- (left) and Fe^{II}_2- (right) NrdF structures. Distances are reported in Å.

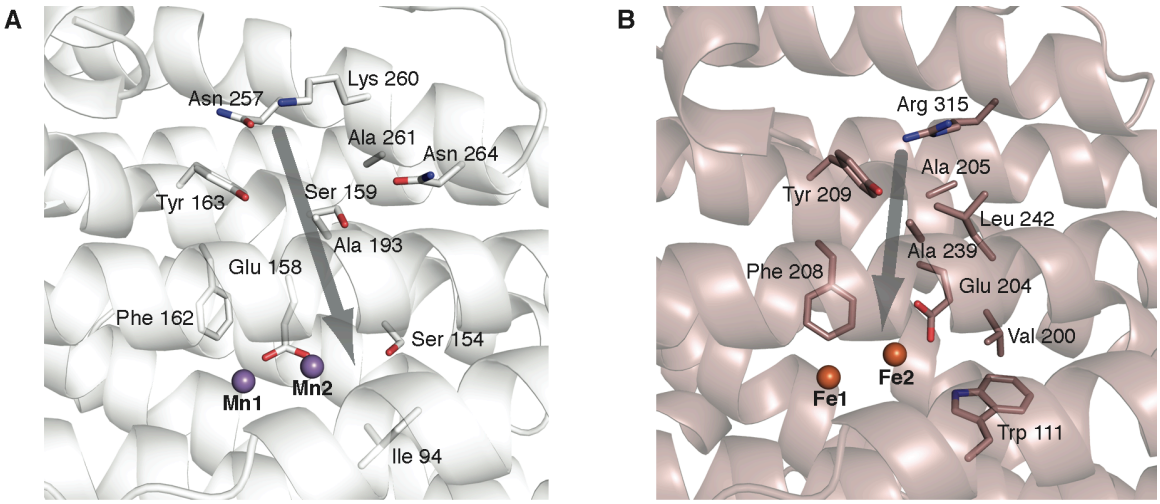

Figure S3. Side-by-side views of the active site channels in Mn^{II}_2-NrdF (class Ib) and Fe^{II}_2-NrdB (class Ia) (PDB code 1PIY). (**A**) Mn^{II}_2-NrdF is shown as a white ribbon diagram and the Mn^{II} ions are shown as purple spheres. Residues lining the active site channel are represented in stick format. The active site channel is indicated by a gray arrow. Ser 154 is shown here as the rotamer that points into the channel cavity. As shown in Fig. 2, it can be modeled in two conformations. (**B**) Fe^{II}_2-NrdB is shown as a pink ribbon diagram and the Fe^{II} ions are shown as orange spheres. Residues lining the active site channel are represented in stick format. The active site channel is indicated by a gray arrow. Glu 204 in NrdB is the equivalent residue to NrdF Glu 158, and is coordinated to Fe2 in a monodentate fashion.

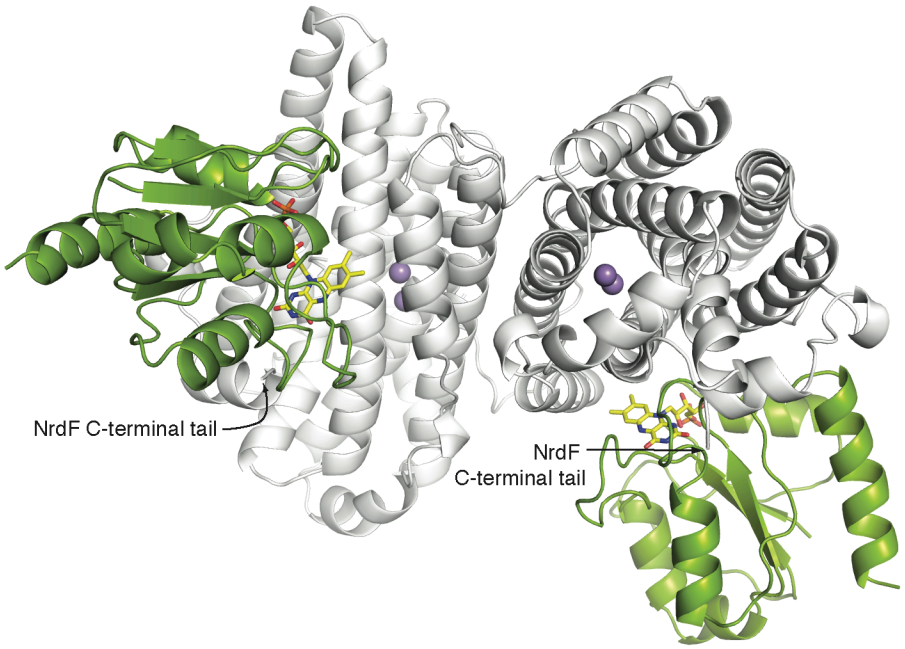

Figure S4. Alternate view of $NrdI_{ox}$/NrdF complex. Mn^{II}_2-NrdF is shown as a white ribbon diagram and the Mn^{II} ions are shown as purple spheres. $NrdI_{ox}$ is shown as a green ribbon diagram and the FMN cofactor is represented in stick format and colored by atom type. The last NrdF residue observed in all NrdI/NrdF complex structures is residue 287 or 288 (out of 319). The final 32 residues are critical for interaction with the α2 subunit (NrdE) and thus for RNR activity. The location of the beginning of the unmodeled C-terminal tail (black arrow in each NrdF monomer) suggests that NrdI and NrdE might occupy unique binding sites on NrdF.

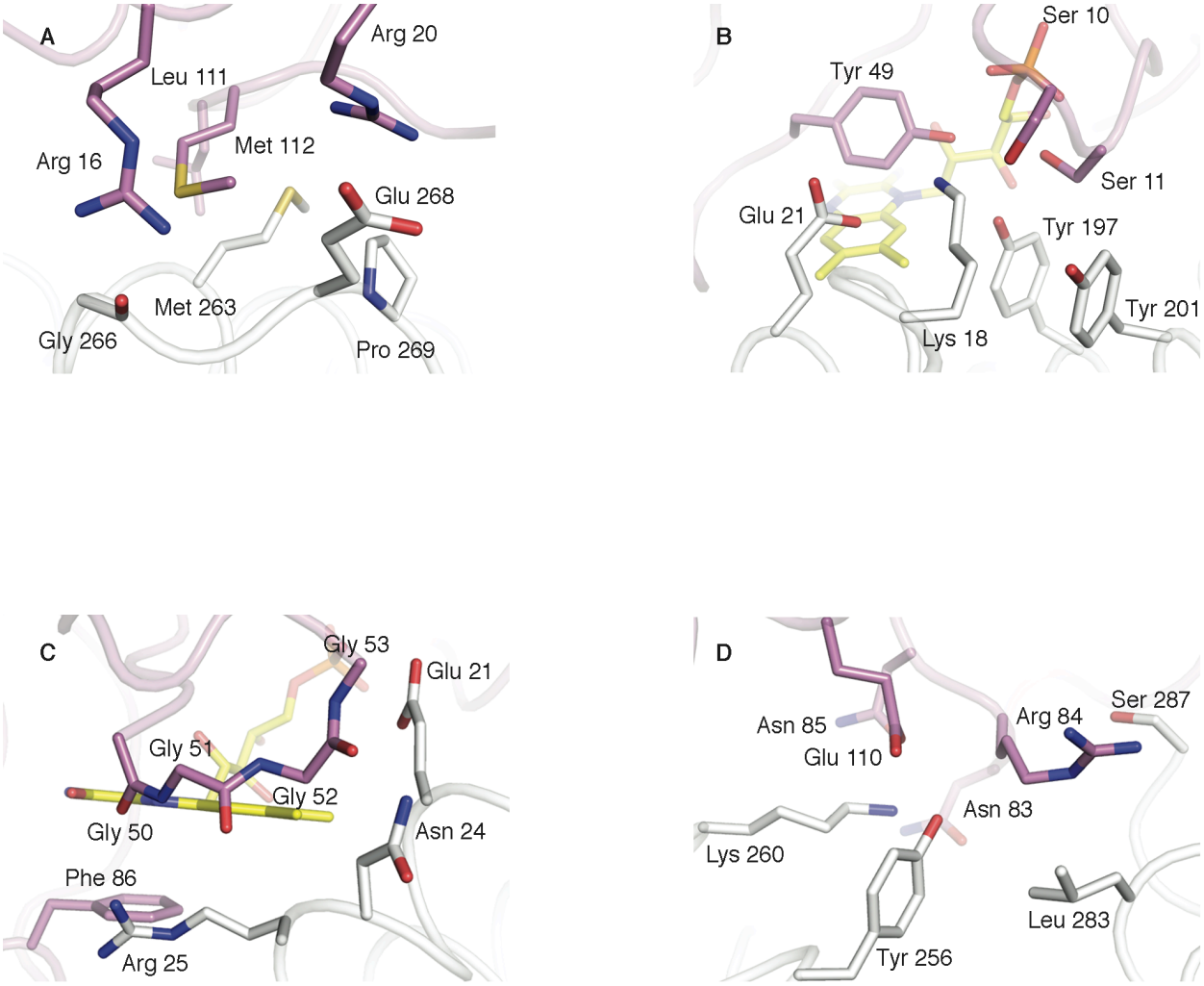

Figure S5. Selected views of the $NrdI_{hq}$/NrdF complex interface. $NrdI_{hq}$ is shown as a purple ribbon diagram and NrdF is shown as a white ribbon diagram. The FMN cofactor and residues at the complex interface are depicted as sticks and colored by atom type. The interfacial regions in the $NrdI_{ox}$/NrdF and $NrdI_{hq}$/$NrdF_{perox}$ structures are largely similar except as shown in Figs. 3B, 3C, S7, and S13. Due to differences in data resolution, ordered solvent and protein side chains on the surface are not uniformly well resolved in the $NrdI_{ox}$/NrdF structure. (**A**) An example of a largely hydrophobic interaction involving NrdF Met 263 and NrdI Leu 111 and Met 112 (left). (**B**) The environment around the FMN cofactor is influenced by both NrdI and NrdF, with residues involved in both potential hydrogen bonding interactions and hydrophobic packing against the dimethylbenzene portion of the FMN isoalloxazine ring. (**C**) Interactions between NrdF, the NrdI 50s loop, and NrdI Phe 86 (shown in greater detail in Fig. 3). (**D**) A conserved hydrogen bonding network (left) located at the active site channel interface (shown in greater detail in Figs. 4, S7, and S11). The final observable C-terminal residue in the NrdF model (Ser 287) is also associated with this site (right).

A

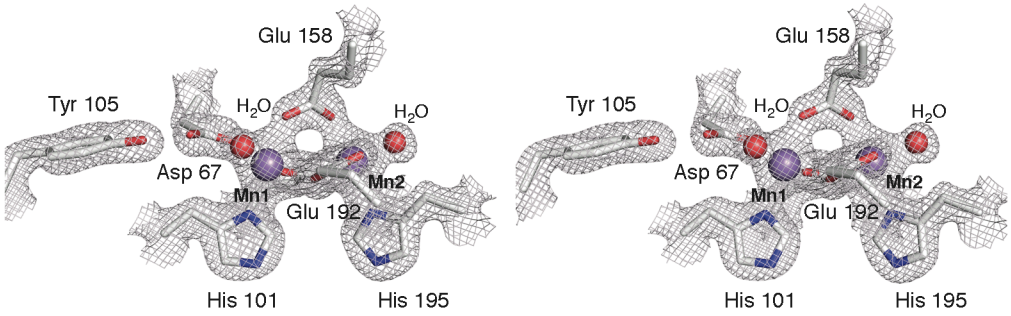

B

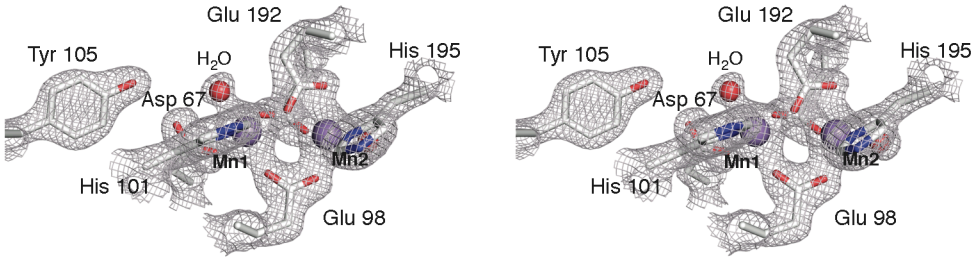

Figure S6. Stereo view of the Mn^{II}_2 active site in $NrdI_{hq}$/NrdF. The structures of the active sites in $NrdI_{ox}$/NrdF and $NrdI_{hq}$/$NrdF_{perox}$ are nearly identical and all three complex structures have the same coordination environment as Mn^{II}_2-NrdF (Figs. 1A, S2). (**A**) A $2F_o$-F_c electron density map (gray mesh, contoured at 1.8 σ) is shown for residues and solvent molecules in the first coordination sphere along with Tyr 105, the site of the stable tyrosyl radical in NrdF. Mn^{II} ions are shown as purple spheres, water molecules are shown as red spheres, and NrdF side chains are represented in stick format and colored by atom type. (**B**) An alternate view of (**A**) highlighting the μ-(η^1,η^2) bridging interaction between Glu 192 and the Mn^{II}_2 site.

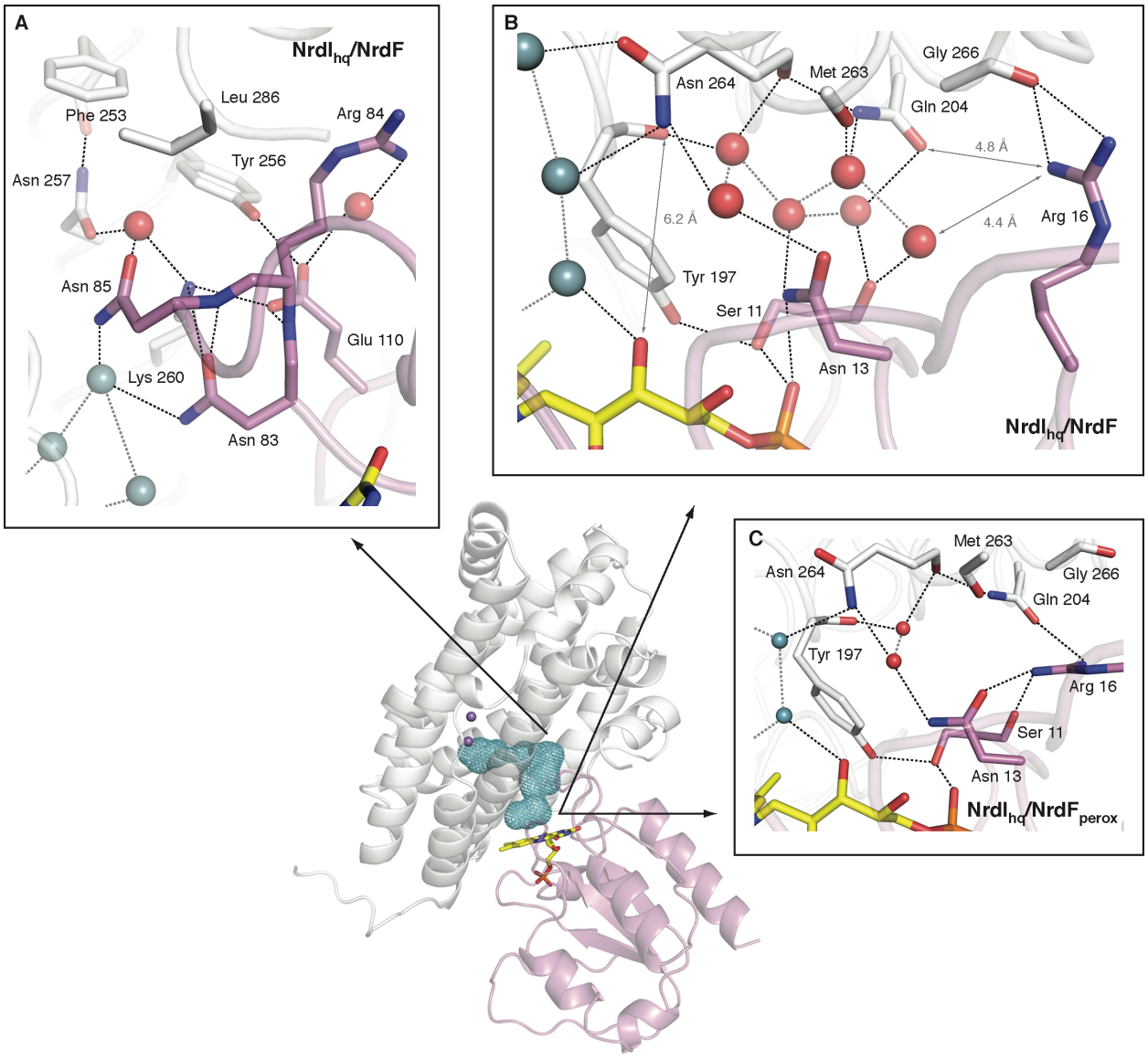

Figure S7. Potential solvent access points in the NrdI/NrdF active site channel. NrdI$_{hq}$ (purple) and NrdF (white) are shown as ribbon diagrams with selected residues represented in stick format and colored by atom type. Ordered waters within the channel are depicted as cyan spheres while those beyond the channel but potentially connected via hydrogen bonding interactions are shown as red spheres. Potential hydrogen bonding interactions involving protein donors/acceptors are indicated by dashed black lines and hydrogen bonding interactions among solvent molecules are drawn in gray dashed lines. (**A**) The corner of the channel defined by residue Lys 260 is surrounded by a hydrogen bonding network that extends to the surface of the protein but does not allow direct solvent access. Asn 85 hydrogen bonds to solvent in the active site channel (lower left) as well as to water molecules in the extended hydrogen bonding network. Direct access to bulk solvent is blocked by residues Phe 253, Tyr 256, and Leu 286. Hydrogen bonds reach the protein surface via interactions linking NrdF Lys 260 to NrdI Glu 110, which is connected to Arg 84 by an intervening water molecule. The last observable residue in NrdF (Ser 287) is in close proximity to this network and the final 32 residues at the NrdF C-terminus remain unmodeled. Thus, the unmodeled tail may itself be

involved in extension of this network or may further prohibit access to bulk solvent. This region is largely the same in $NrdI_{ox}$/NrdF except that ordered solvent is not well resolved. (**B**) An intricate water-mediated hydrogen bonding network is evident along the NrdI/NrdF interface extending away from the channel mouth at the NrdI FMN cofactor. This chain of solvent molecules is not directly hydrogen-bonded to solvent in the active site channel (left). However, interaction between the two water reservoirs occurs via NrdF Asn 264 and a ~6 Å cavity exists between the two that may provide sufficient physical space for solvent exchange. The solvent along the interface is tightly hydrogen-bonded to other solvent molecules, to backbone carbonyl oxygen atoms from both NrdI and NrdF residues, and to the side chains of NrdI Asn 13, NrdF Asn 264 and NrdF Gln 204. Water molecules centrally located among strongly directional donors and acceptors such as these result in a highly oriented solvent network reminiscent of that in aquaporin structures (*S14*). Such networks are proposed to increase the free energy barrier for proton conduction (*S15*). Interaction of NrdI Arg 16 with the backbone carbonyl oxygen atom of NrdF Gly 266, also similar to a key interaction found at the conducting pore in aquaporin structures (*S14*), creates a ~5 Å cavity separating the solvent network from the protein exterior. (**C**) The analogous network to that shown in (**B**) for the $NrdI_{hq}$/$NrdF_{perox}$ structure. Here NrdI Arg 16 adopts a different conformation and is engaged in hydrogen bonding interactions with NrdF Gln 204 and NrdI Asn 13 and Ser 11 residues.

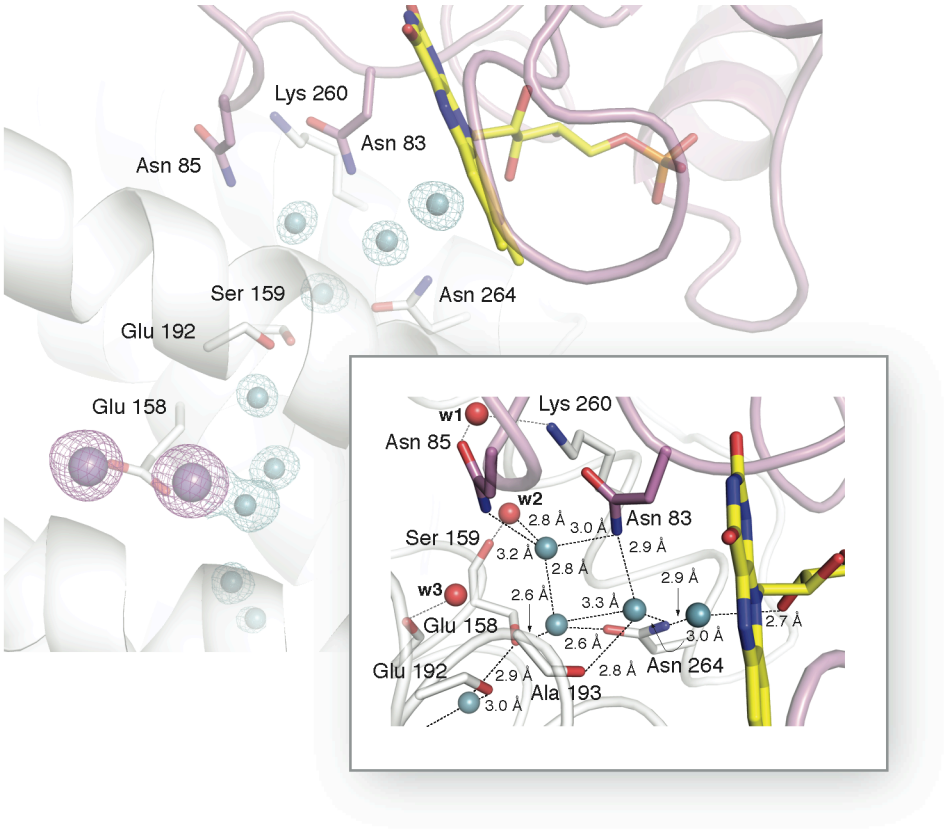

Figure S8. The $NrdI_{hq}$/NrdF active site channel terminating at Mn2. $NrdI_{hq}$ (purple) and NrdF (white) are shown as ribbon diagrams. Residues and backbone atoms lining the interfacial region of the channel are highlighted in stick format. A $2F_o$-F_c electron density map (cyan mesh, contoured at 1.2σ) shows ordered waters in the channel. The Mn anomalous difference Fourier map (purple mesh, contoured at 9σ) is also shown. Water molecules within the channel cavity are represented as cyan spheres whereas water molecules implicated in the extended hydrogen bonding network are shown as red spheres and labelled w1, w2, and w3 (Fig. S11). Potential hydrogen bonding interactions involving ordered solvent in the channel are illustrated with dashed lines in the inset. The location of these waters and their hydrogen bonding interactions with residues lining the channel delineate the explicit path that the oxidant might take as it navigates the channel. In one NrdI/NrdF subunit, electron density for two of these waters is not observed, indicating they are disordered or not fully occupied. Notably, these specific waters occupy the putative peroxide binding site in the $NrdI_{hq}$/$NrdF_{perox}$ structure. The differences between a peroxide oxidant and a given pair of hydrogen bonded solvent molecules (e.g. O-O bond distance) may drive fast and directional migration of the oxidant to the active site. Furthermore, the water network itself may maintain the structure of the channel such that it is primed to transport the oxidant efficiently and could also fulfill unsatisfied hydrogen bonding interactions left in the wake of its passage.

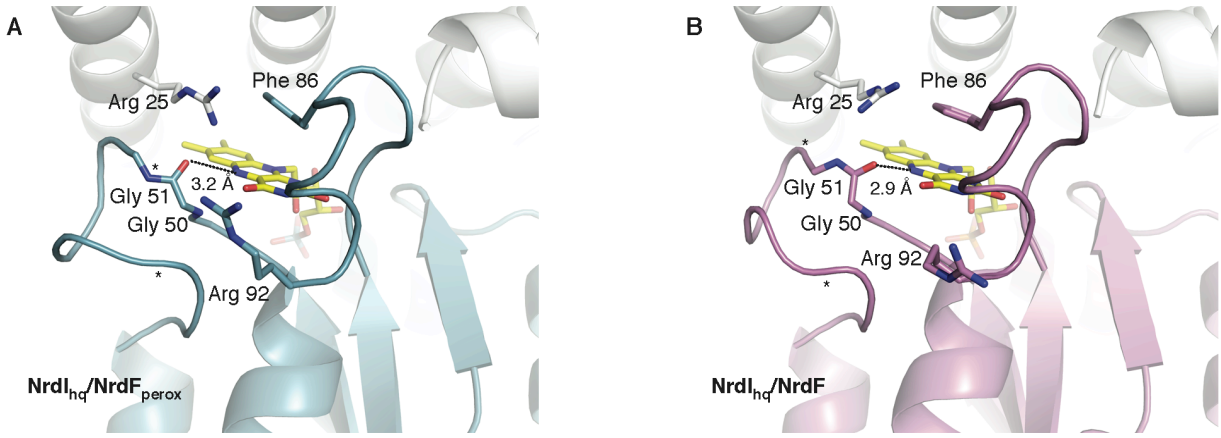

Figure S9. A comparison of the 50s loop orientation in the NrdI$_{hq}$/NrdF$_{perox}$ and NrdI$_{hq}$/NrdF structures. (**A**) In the NrdI$_{hq}$/NrdF$_{perox}$ structure, NrdI is shown as a blue ribbon diagram and NrdF is shown as a white ribbon diagram with the FMN cofactor and selected residues represented in stick format and colored by atom type. A dashed line indicates a potential hydrogen bonding interaction between the NrdI 50s loop (far left NrdI loop) and the N5 position of the FMN isoalloxazine ring (note that this position is immediately adjacent to the O_2 reaction site (C4a) located between the N5 position and the C4 carbonyl moiety). Asterisks denote the region of the loop for which discontinuous electron density was observed. (**B**) In the NrdI$_{hq}$/NrdF structure, NrdI is shown as a purple ribbon diagram and NrdF is shown as a white ribbon diagram with the FMN cofactor and selected residues represented in stick format and colored by atom type. A dashed line indicates a potential hydrogen bonding interaction between the NrdI 50s loop (far left NrdI loop) and the N5 position of the FMN isoalloxazine ring. Asterisks denote the region of the loop for which discontinous electron density was observed.

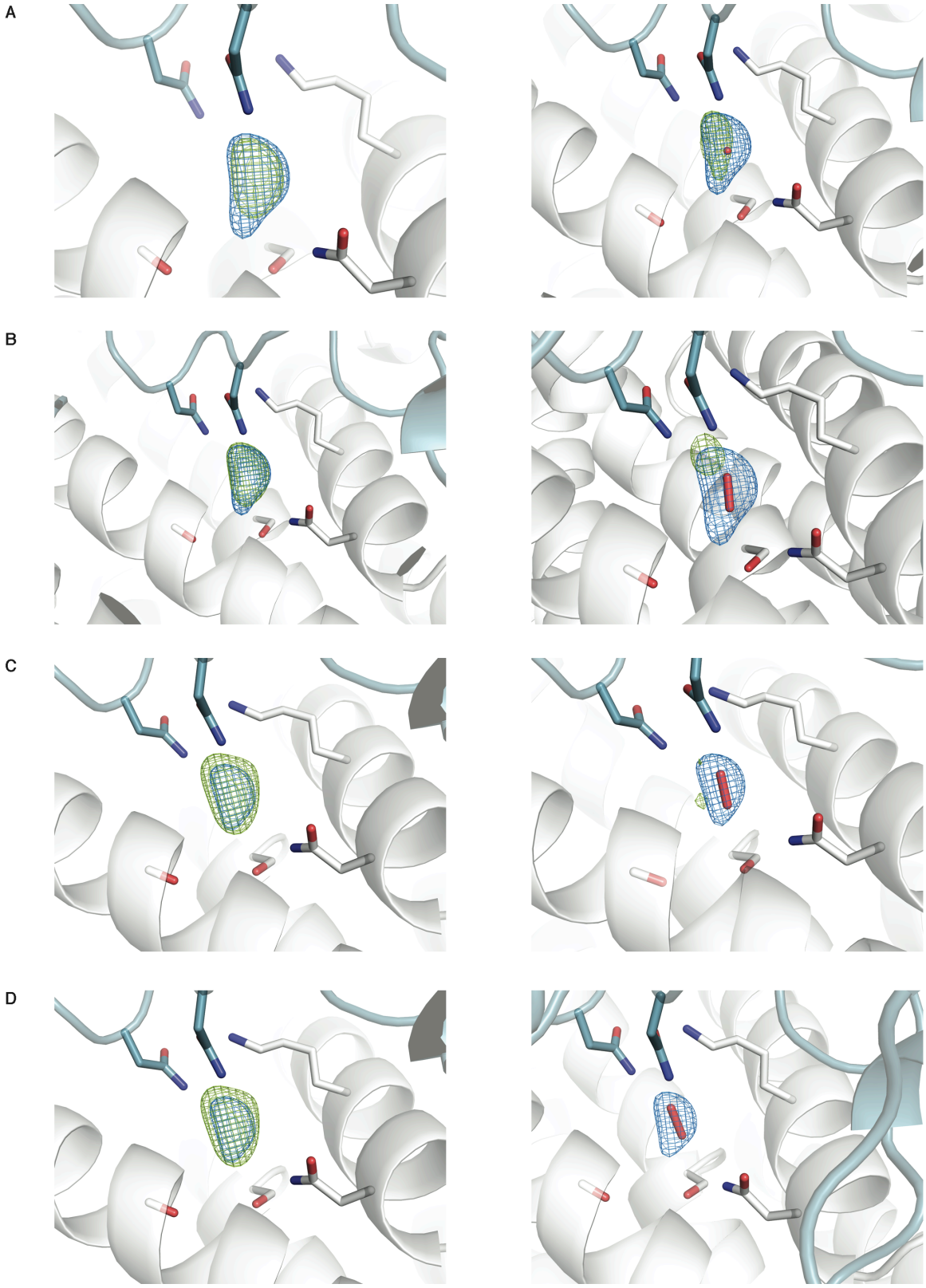
A
B
C
D

E

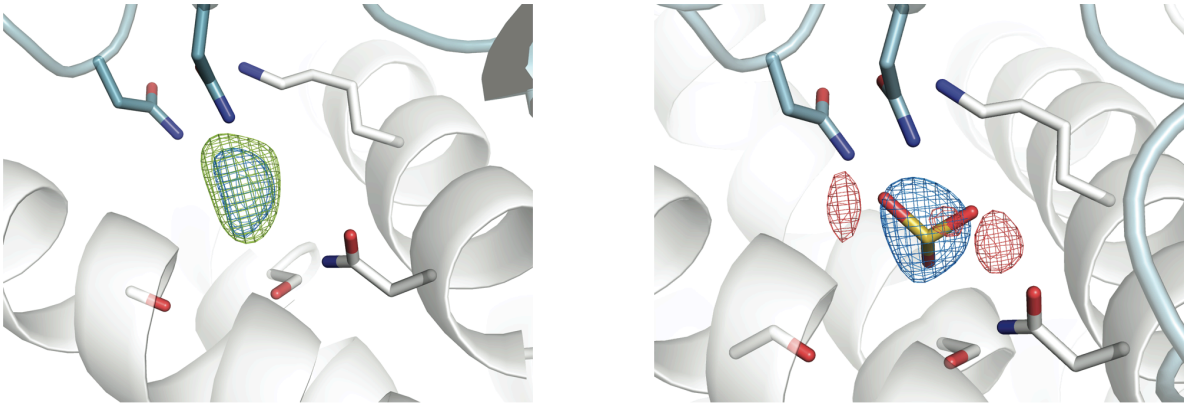

Figure S10. Alternative models for the unexplained density in $NrdI_{hq}/NrdF_{perox}$. In all panels, a $2F_o$-F_c electron density map (blue mesh, contoured at 1.2σ (**A**, **B**) or 1.8σ (**C**, **D**)) is shown for the unmodeled density found in the active site channel after the first refinement cycle. (**A**) F_o-F_c density (green mesh, contoured at 3.7σ) is shown for the map obtained after the first refinement cycle (left) and after modeling as a single water molecule (right). (**B**) F_o-F_c density (green mesh, contoured at 2.8σ) after the first refinement cycle (left) and after modeling as dioxygen (right) (O-O bond distance = 1.2 Å). (**C**) F_o-F_c difference density (green mesh, contoured at 2.8σ) after the first refinement cycle (left) and after modeling as superoxide (right) (O-O bond distance = 1.34 Å). (**D**) F_o-F_c difference density (green mesh, contoured at 2.8σ) after the first refinement cycle (left) and after modeling as peroxide (right) (O-O bond distance = 1.47 Å). **(E**) F_o-F_c difference density (green or red mesh, contoured at 2.8σ or -2.8σ, respectively) after the first refinement cycle (left) and after modeling as sulfite (right).

A

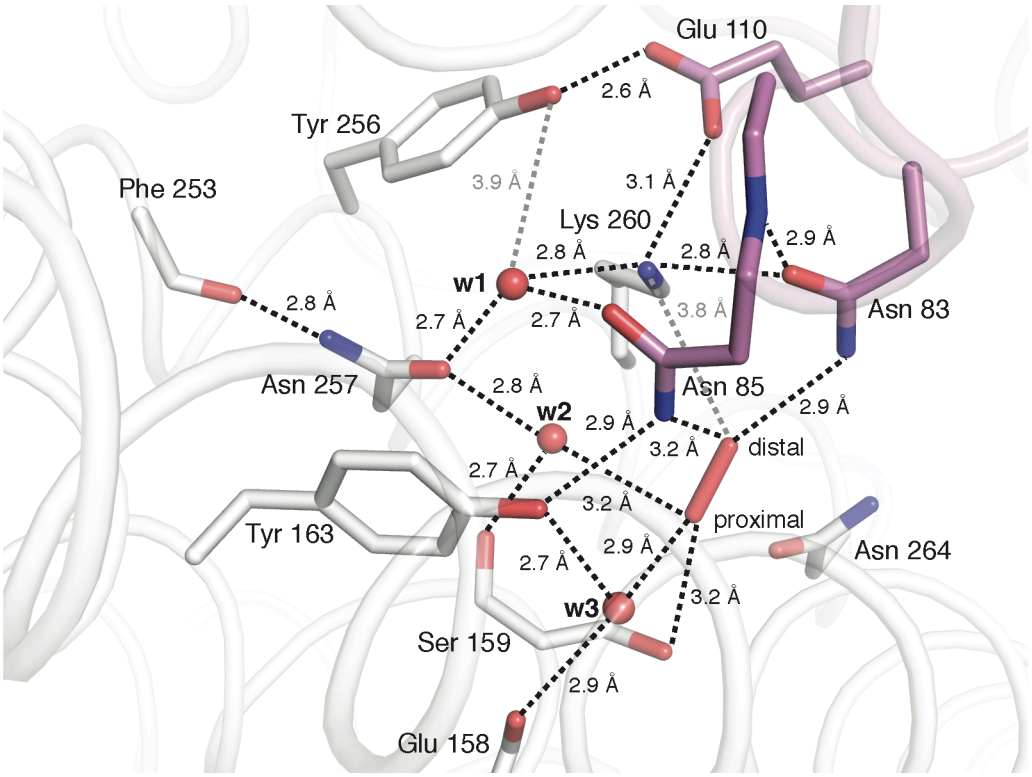

Figure S11. The details of the extended hydrogen bonding network near the modeled peroxide binding site. Analysis of this network supports the proposal that the oxidant exists in a specific protonation state (*S10*) and provides evidence for its orientation within this site. $NrdI_{hq}$ (purple) and NrdF (white) are shown as ribbon diagrams with selected residues represented in stick format and colored by atom type. The peroxide species is shown as a red stick and ordered waters in the network are depicted as red spheres and labeled w1, w2, and w3. Potential hydrogen bonding interactions are indicated by dashed black lines and long-range interactions are drawn in gray dashed lines. The NrdF residues involved in this network are universally well conserved. (**A**) In one subunit, the distal oxygen of the modeled peroxide hydrogen bonds asymmetrically to the NrdI Asn residues, forming a tighter interaction with the water molecules near the the proximal oxygen.

B

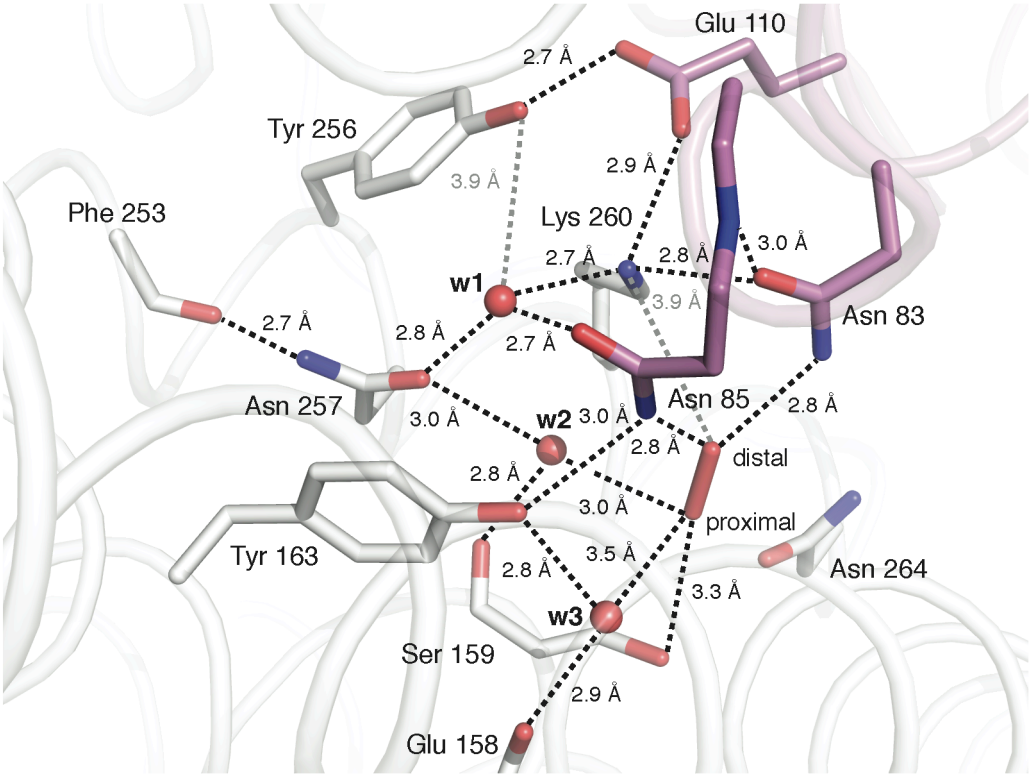

Figure S11. (cont'd) (**B**) In the other subunit, the distal oxygen of the modeled peroxide binds more symmetrically to the NrdI Asn residues, resulting in a weaker interaction with w3. Slight differences in interatomic distances are observed throughout the network when comparing the two subunits and may reflect the dynamics of the trapped species within this site. The modeled peroxide sits directly above the channel constriction defined by Ser 159 and the backbone carbonyl of Glu 192, which may provide an explanation for observation of a peroxide species at this site. The point of constriction may serve as the final orientation filter before reaction of the oxidant with the metal site. Since residues at this constriction are closely linked to Mn2 ligands Glu 158 and Glu 192, passage of the oxidant through this checkpoint could induce ligand conformational changes or vice versa. However, there are not obvious conformational differences between $NrdI_{hq}/NrdF_{perox}$ and the other complex structures in this region. It is possible that the peroxide is stalled because some conformational flexibility is precluded in the crystal. Alternatively, the water network may not be appropriately configured for oxidant delivery. It is also conceivable that the trapped species is in an incorrect protonation state (if the density originated from reaction of dithionite and O_2 rather than from reaction of $NrdI_{hq}$ with O_2). While the proximity of the sole positively charged residue within the channel (Lys 260, ~4 Å) and the presence of two strongly directional hydrogen bond donors (NrdI Asn 83 and Asn 85) near the distal peroxide O atom suggest that the site could optimally interact with HO_2^-, the protonation state of the distal O atom in the modeled peroxide cannot be determined unambiguously.

C

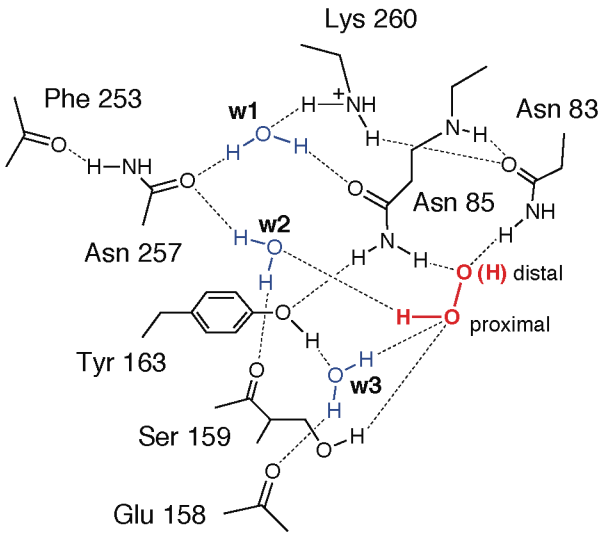

Figure S11 (cont'd). (**C**) A schematic drawing, including protons, of the hydrogen bonding network in $NrdI_{hq}/NrdF_{perox}$ as shown in Fig. S11A and B. Ordered solvent is shown in blue and the modeled peroxide is shown in red. Hydrogen bonding interactions are illustrated as dashed lines. As drawn, Asn 85 and Asn 83 each donate a hydrogen bond to a HO_2^- or H_2O_2 peroxide species. The conformation of Asn 85 cannot be assigned definitively, but the rotamer depicted is favored based on computational analysis (*S16*).

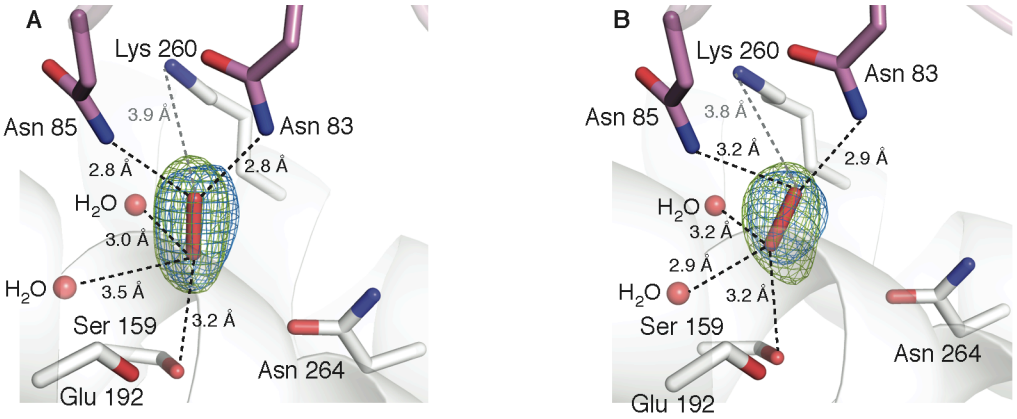

Figure S12. The electron density modeled as a peroxide species in each subunit of the $NrdI_{hq}/NrdF_{perox}$ structure. (**A**) and (**B**) show the differences in the shape of the density in each subunit as well as slight alterations in the hydrogen bonding interactions with nearby residues and water molecules (see Fig. S11 for greater detail). The two different orientations of the modeled peroxide and the surrounding hydrogen bonding network suggest that the oxidant may move through the channel by alternating between transient hydrogen bonding interactions.

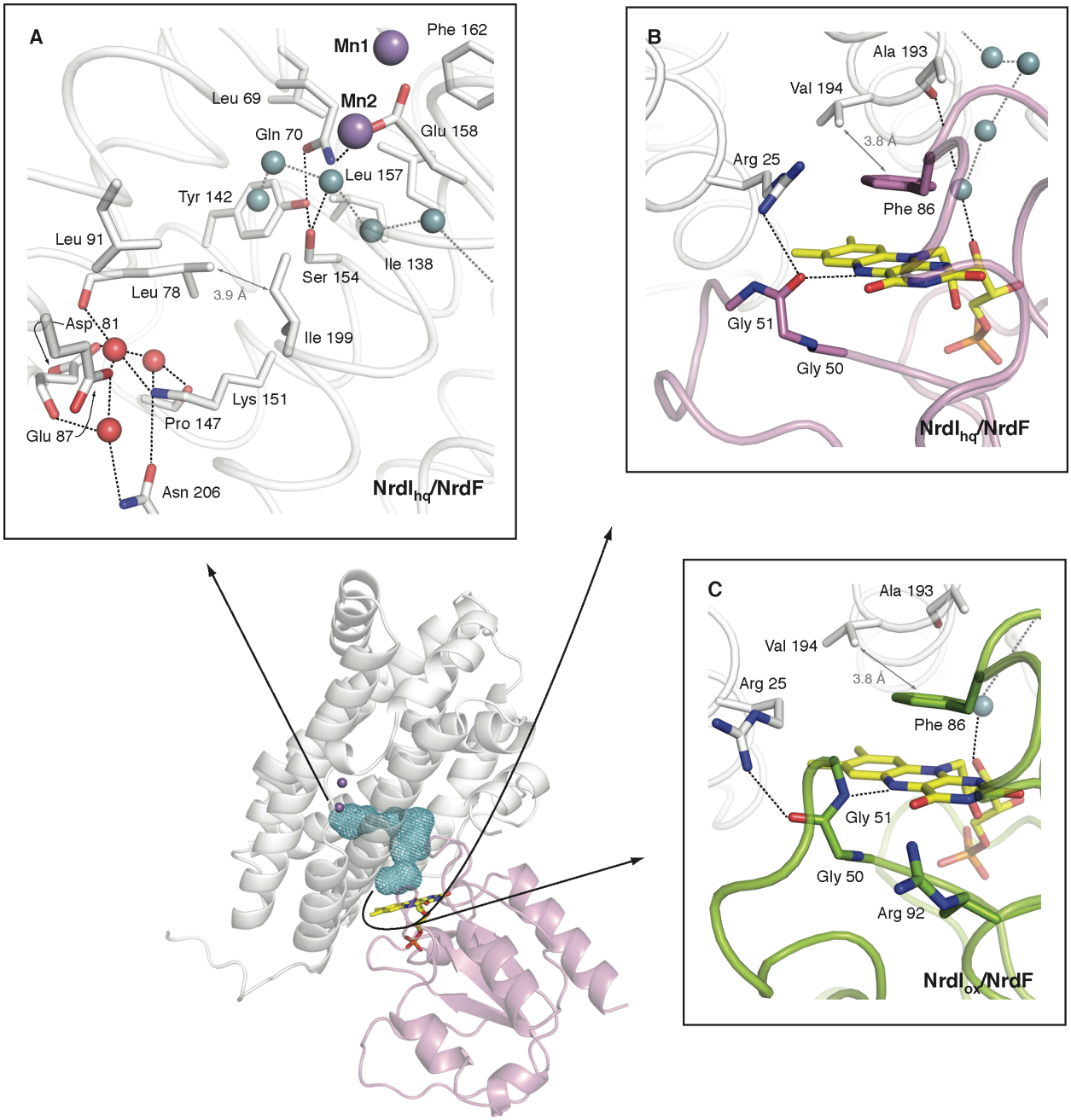

Figure S13. Potential solvent access points in the NrdI/NrdF active site channel. NrdI$_{hq}$ (purple), NrdI$_{ox}$ (green), and NrdF (white) are shown as ribbon diagrams with selected residues represented in stick format and colored by atom type. Ordered waters within the channel are depicted as cyan spheres while those beyond the channel but potentially connected via hydrogen bonding interactions are shown as red spheres. Potential hydrogen bonding interactions involving protein donors/acceptors are indicated by dashed black lines and hydrogen bonding interactions among solvent molecules are drawn in gray dashed lines. (**A**) Solvent access at the terminus of the channel is precluded by hydrophobic residues Leu 78 and Ile 199. A hydrogen bonding network connects the solvent molecule coordinated to Mn2 to bridging ligand Glu 158 (Fig. 2), but extension of the network is prevented by the positions of residues Leu 69, Ile 138, Leu 157, and Phe 162. (**B**) (**C**) Solvent access at the mouth of the

channel is blocked by hydrophobic residues NrdI Phe 86 and NrdF Val 194. Hydrogen bonding interactions immediately outside the channel as well as those within it may control oxidant access to the channel. The interaction with the flavin N5 atom and hydrogen bonds linking the carbonyl oxygens of Gly 50 and Gly 52 to the side chain of NrdF Arg 25 and NrdI Arg 92, respectively, likely constrain the loop position so that it blocks access to the reactive C4a position of the isoalloxazine ring, which may be important in preventing diffusion of the proposed oxidant (HO_2^-) into solution after it is produced. A comparison of the $NrdI_{hq}$/NrdF and $NrdI_{ox}$/NrdF structures provides some insight into how the putative HO_2^- might move from its site of production near the flavin C4a position to the mouth of the channel. It is likely that O_2 accesses the C4a position of the flavin in the $NrdI_{hq}$/NrdF complex from the *si* face (closest to Phe 86). It may be reduced by two electrons and protonated by N5H upon oxidation of the flavin. Interestingly, there appears to be no other nearby source of a second proton to form H_2O_2. The released oxidant could be electrostatically attracted by NrdF Arg 25 towards the channel. Arg 25 is also pulled away from the ring by its nascent hydrogen bonding interaction with the carbonyl of Gly 50, allowed by the conformational change in the loop accompanying flavin oxidation and deprotonation of N5. Together, these concerted conformational changes may facilitate entrance of the oxidant while keeping the channel inaccessible to solvent.

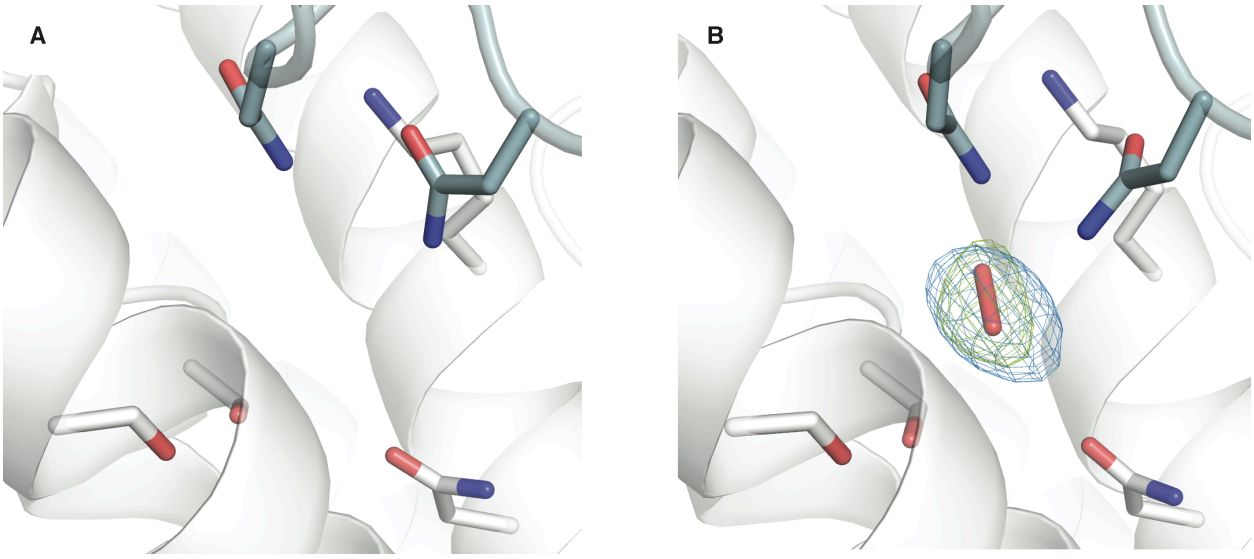

Figure S14. Electron density in the active site channel for anaerobically (**A**) and aerobically (**B**) dithionite soaked (100 mM) NrdI/NrdF crystals. A $2F_o$-F_c electron density map (blue mesh, contoured at 2.0σ) is shown for the unmodeled density found in the active site channel after the first refinement cycle. F_o-F_c density (green mesh, contoured at 2.8σ) is shown for the map obtained after the first refinement cycle. No density is found in this location for the anaerobically soaked crystal. The anaerobic dithionite soak (**A**) resulted in uniformly low resolution (>3.5 Å, data shown here is 3.5 Å resolution) that could not be improved. The view in (**B**) is a $NrdI_{ox}$/NrdF aerobically dithionite-soaked structure of similar resolution (3.3 Å). Repeating the aerobic dithionite soak protocol on multiple crystals always yielded strong electron density in the same location in the channel. In some cases, the FMN environment resembled that in $NrdI_{ox}$/NrdF, but only the $NrdI_{hq}$/$NrdF_{perox}$ crystals diffracted to better than 2.9 Å resolution.

Table S1. Data collection and refinement statistics for NrdF structures

	Mn^{II}_2-NrdF (native)	Mn^{II}_2-NrdF (anomalous)	Fe^{II}_2-NrdF (native)	Fe^{II}_2-NrdF (anomalous)
Data collection				
Wavelength (Å)	0.98	1.85	1.03	1.72
Space group	$P6_522$	$P6_522$	$P6_522$	$P6_522$
Cell dimensions				
a, *b*, *c* (Å)	78.14, 78.14, 266.75	78.21, 78.21, 267.19	79.14, 79.14, 267.98	79.08, 79.08, 268.39
Wavelength (Å)	0.98	1.85	1.03	1.72
Resolution (Å)	50.0-1.65 (1.68-1.65)	50.0-2.33 (2.37-2.33)	50.0-1.90 (1.93-1.90)	50.0-2.20 (2.24-2.20)
R_{sym} or R_{merge}	0.059 (0.605)	0.064 (0.150)	0.079 (0.618)	0.098 (0.580)
$I / \sigma I$	30.5 (2.2)	35.4 (23.6)	36.2 (2.0)	30.5 (2.4)
Completeness (%)	96.9 (95.1)	95.1 (92.8)	97.5 (72.9)	99.5 (92.4)
Redundancy	7.3 (7.0)	16.4 (16.9)	18.0 (7.8)	16.8 (5.6)
Refinement				
Resolution (Å)	50.0-1.65		50.0-1.90	
No. reflections	54457		36996	
R_{work} / R_{free}	0.167/0.186		0.196/0.220	
No. atoms	2799		2487	
Protein	2391		2331	
Ligand/ion	8		2	
Water	400		154	
B-factors				
Protein	11.6		27.2	
Ligand/ion	38.7		36.7	
Water	26.1		32.8	
R.m.s. deviations				
Bond lengths (Å)	0.009		0.009	
Bond angles (°)	1.09		1.004	

Table S2. Data collection and refinement statistics for NrdI/NrdF complex structures

	$NrdI_{ox}$/NrdF (native)	$NrdI_{hq}$/NrdF (native)	$NrdI_{hq}$/NrdF (anomalous)	$NrdI_{hq}$/$NrdF_{perox}$ (native)
Data collection				
Wavelength (Å)	1.08	1.08	1.85	1.08
Space group	$P2_12_12_1$	$P2_12_12_1$	$P2_12_12_1$	$P2_12_12_1$
Cell dimensions				
a, *b*, *c* (Å)	75.40, 90.72, 143.79	74.86, 90.68, 143.84	75.06, 90.70, 143.95	75.72, 91.35, 144.11
Resolution (Å)	50.0-2.50 (2.50-2.54)	50.0-2.00 (2.03-2.00)	30.0-2.40 (2.44-2.40)	50.0-2.35 (2.39-2.35)
R_{sym} or R_{merge}	0.095 (0.373)	0.084 (0.641)	0.116 (0.837)	0.122 (0.476)
$I / \sigma I$	12.4 (2.4)	23.6 (3.0)	17.8 (3.0)	10.9 (2.2)
Completeness (%)	91.4 (68.1)	100.0 (100.0)	100.0 (99.9)	93.2 (81.9)
Redundancy	4.0 (3.0)	7.4 (7.4)	7.0 (6.5)	4.4 (2.8)
Refinement				
Resolution (Å)	50.00-2.50	50.00-2.00		50.00-2.35
No. reflections	29768	63605		37194
R_{work} / R_{free}	0.235/0.273	0.203/0.227		0.234/0.275
No. atoms	6680	6973		6891
Protein	6594	6627		6653
Ligand/ion	66	66		70
Water	20	280		168
B-factors				
Protein	28.9 (NrdF)	21.2 (NrdF)		20.9 (NrdF)
	43.2 (NrdI)	30.6 (NrdI)		34.2 (NrdI)
Ligand/ion	43.0 (37.6)	27.6 (21.7)		23.8 (21.4)
Water	20.2	26.7		22.9
R.m.s. deviations				
Bond lengths (Å)	0.006	0.009		0.006
Bond angles (°)	0.856	1.054		0.817

References

S1. Z. Otwinowski, W. Minor, *Methods Enzymol.* **276**, 307 (1997).

S2. A. J. McCoy, R. W. Grosse-Kunstleve, L. C. Storoni, R. J. Read, *Acta Cryst.* **D61**, 458 (2005).

S3. P. Emsley, K. Cowtan, *Acta Cryst.* **D60**, 2126 (2004).

S4. G. N. Murshudov, A. A. Vagin, E. J. Dodson, *Acta Cryst.* **D53**, 240 (1997).

S5. R. A. Laskowski, *J. Appl. Cryst.* **26**, 283 (1993).

S6. A. A. Vaguine, J. Richelle, S. J. Wodak, *Acta Cryst.* **D55**, 191 (1999).

S7. W. L. Delano, *The PyMOL molecular graphics system*. (DeLano Scientific, San Carlos, CA, 2002).

S8. B. K. Ho, F. Gruswitz, *BMC Struct. Biol.* **8**, 49 (2008).

S9. J. A. Cotruvo, Jr., J. Stubbe, *Proc. Natl. Acad. Sci. USA* **105**, 14383 (2008).

S10. J. A. Cotruvo, Jr., J. Stubbe, *Biochemistry* **49**, 1297 (2010).

S11. M. Eriksson, A. Jordan, H. Eklund, *Biochemistry* **37**, 13359 (1998).

S12. M. Högbom, Y. Huque, B.-M. Sjöberg, P. Nordlund, *Biochemistry* **41**, 1381 (2002).

S13. W. C. Voegtli *et al.*, *J. Am. Chem. Soc.* **125**, 15822 (2003).

S14. J. D. Ho *et al.*, *Proc. Natl. Acad. Sci. USA* **106**, 7437 (2009).

S15. B. Ilan, E. Tajkhorshid, K. Schulten, G. A. Voth, *Proteins* **55**, 223 (2004).

S16. I. W. Davis *et al.*, *Nucleic Acids Res.* **35**, W375 (2007).